Schwann Cell Contact Guidance versus Boundary Interaction in Functional Wound Healing along Nano and Microstructured Membranes

Ilaria Tonazzini,* Emanuela Jacchetti, Sandro Meucci, Fabio Beltram, and Marco Cecchini

1. Introduction

Nerves form a very complex web throughout the body that connects the central nervous system and the sensory and autonomic ganglia to the peripheral target organs of the motor and sensory pathways. [1] Peripheral nerve lesions have a rather high incidence with a negative impact on the quality of life of affected individuals and significant healthcare and social costs. This motivates a large interest from both basic and clinical research on the study of nerve repair and regeneration.[2]

Compared to the central nervous system, peripheral nerve fibers retain a higher post-traumatic regeneration potential. Although advances in surgical techniques and in repair methods (e.g., the use of autologous nerve grafts; biological or synthetic tubulizations; autologous cell-transplant therapies)[3–5] have brought significant improvements, in most cases the clinical outcome after peripheral nerve lesions is still far from being satisfactory and functional recovery is very seldom complete.[6,7] Today artificial scaffolds are used only for short gaps and with poor functional recovery while the use of cell-transplant therapies, although appealing, still presents issues related to the limited autologous Schwann cell (SC) availability or to the safety of pluripotent or multipotent cell use.[7] Despite recent developments in biomaterial-based artificial scaffolds,[8] autografting (with the related donor-site morbidity) still remains the gold standard in the clinical practice for nerve reconstruction.[3,7]

Artificial scaffolds can provide a guidance and mechanical support, reduce scar formation and, importantly, do not require the extraction of healthy tissue from the patient. In this scenario, the detailed knowledge of the mechanisms on the basis of nerve cell–material interactions is of pivotal importance since it is a prerequisite for a rational design of optimal nerve scaffolds.

Contact guidance describes the phenomenon by which cells respond to the extracellular nanotopography by adapting their morphology, orientation, and/or motility.[9,10] One promising approach relies on the exploitation of nano/microengineering techniques to produce nanostructured surfaces, which were shown to be capable of tuning neuronal and glial cell

Dr. I. Tonazzini, Dr. E. Jacchetti, Dr. S. Meucci,
Prof. F. Beltram, Dr. M. Cecchini
NEST, Scuola Normale Superiore
PiazzaSanSilvestro12 , Pisa 56127, Italy
E-mail: ilaria.tonazzini@sns.it

Dr. I. Tonazzini, Dr. E. Jacchetti, Dr. S. Meucci,
Prof. F. Beltram, Dr. M. Cecchini
NEST, Istituto Nanoscienze-CNR
PiazzaSanSilvestro12 , Pisa 56127, Italy
Dr. I. Tonazzini
Fondazione Umberto Veronesi
PiazzaVelasca5 , Milano 20122, Italy

differentiation, polarity, migration, neurite orientation,[11–18] and even stem cell fate.[19,20] Nano/microgratings (GRs), anisotropic topographies composed by alternating lines of grooves and ridges with lateral dimension typically down to hundreds of nanometers, are a category of substrates that were intensively investigated and are often considered the most effective geometry to induce cell alignment and directional migration based on cell-contact interaction only.[21–25]

SCs are glial cells ensheathing peripheral nerve axons that play a primary role during regeneration of injured peripheral nerves. SC migration from the proximal stump is one of the first physiological mechanisms promoting the regeneration process. After injury, SCs proliferate to form Büngner bands that help the regrowing axons to elongate growth cones in the direction of denervated targets.[26] In fact, during regeneration SCs create a suitable environment for guiding axonal growth by expressing specific cell-adhesion molecules and secreting growth factors.[27] Consequently, SC control in proximity of the lesion can be a useful target to enhance nerve repair.

Here, we interface SCs with microstructured GRs of varying periodicity. Polydimethylsiloxane (PDMS)[28,29] GRs were developed with different lateral periods and depths, leading to two distinct cell–substrate interaction regimes: contact guidance (grating period < cell body diameter, obtained for T1 and T4) and boundary guidance (grating period ≥ cell body diameter, obtained for T20).

By using bright-field and high-resolution fluorescence microscopy on living and fixed cells, we quantitatively investigated the effect of topography on SC morphology, cytoskeleton organization, single-cell migration, and wound-healing capabilities. Finally, we examined SC intercellular coupling by scanning electron microscopy (SEM) imaging and by studying the expression of the neural calcium-dependent cell-adhesion molecule cadherin (N-Cadherin (N-Cad)), a protein that mediates cell–cell and cell–extracellular matrix adhesion, and triggers intracellular signaling cascades to promote migration and axon outgrowth and alignment as well.[30,31]

We show that boundary guidance leads to the best single-cell polarization, actin organization, and single-cell directional migration while contact guidance is instead more effective in driving collective SC migration and can improve functional wound healing. We finally demonstrate that SCs on large-period GRs are characterized by N-Cadherin downregulation and enhanced single-cell scattering into the wound with respect to SCs developing on small-period GRs.

2. Experimental Section

PDMS Grating Scaffolds Fabrication: PDMS membranes were fabricated by replica molding on nano/micropatterned molds. Three GRs with different periodicity ($p = 2w$, w = ridge width = groove width) and depth (h) were produced: T1 ($p = 1$ µm and $h = 0.35$ µm), T4 ($p = 4$ µm and $h = 0.85$ µm), and T20 ($p = 20$ µm and $h = 2.5$ µm). Molds with T1 geometry were fabricated by electron beam lithography (EBL) and dry-etching techniques.[32] Molds with T4 and T20 geometries were fabricated by EBL on a thin polymeric layer (SU-8 2000, MicroChem). Control surfaces (named FLAT) were fabricated

using unpatterned silicon wafers (SYLTRONIX, France) as molds. PDMS replicas were fabricated by mixing prepolymer and curing agent at a ratio of 10:1 by weight, degassing the mixture to remove air bubbles and spin-coating it onto the molds. In order to obtain a film with a thickness of 170 ± 20 µm, the PDMS was spin-coated for 4 min at 300 rpm, left resting for 10 min in order to reduce surface inhomogeneity and thermally cured (at least 60 min at 80 °C). Following removal from the master using a scalpel, PDMS replica were carefully analyzed by optical microscopy, scanning electron microscopy, and surface probe profilometry. For all the topographies, surface and edge roughness were negligible if compared to the main topographic features present on the substrates, and no relevant differences related to the fabrication process were revealed. Our fabrication method produced substrates suitable for bright-field microscopy with highly reproducible micropatterns over macroscopic areas (1 cm^2). Before cell culturing, samples were sterilized by treatment with ethanol (for 15 min at least) and then rinsed with H_2O. The resulting PDMS membranes were first coated with poly-L-lysine (PLL 0.01%, at room temperature for 30 min; P4832, Sigma) and then with laminin (50 µg mL^{-1}, at 37 °C for 30 min) for proper cell adhesion.

Schwann Cell Culture: All experiments involving animals were performed with the approval of local Institution's Animal Care and Ethics Committee and in accordance with the Italian (DL 116/1992) and European Community Council Directives (86/609/EEC). Primary SC cultures were established from sciatic nerves of adult Wistar rats, as in ref. [33]. Briefly, nerves were removed, desheathed, and incubated in culture medium for two weeks: then tissues were dissociated by collagenase and dispase and cultured in poly-D-lysine coated (100 µg mL^{-1}; P0899, Sigma) standard culture plates. SCs were maintained in the presence of glial growth factor (GGF 63 ng mL^{-1}; SRP3055, Sigma) and Forskolin (10×10^{-6} M; F3917, Sigma) in Dulbecco's modified eagle medium (DMEM) supplemented with 10% Fetal Bovine Serum (FBS), 4×10^{-3} M L-glutamine, and antibiotics. Cells were immunodepleted by anti-rat CD90 antibody (1:500, MCA04G; AbD Serotec) to reduce the presence of fibroblasts. SCs (within the tenth passage) were cultured until subconfluence, and then harvested for cell tests. SCs were seeded on PDMS membranes at density of 8×10^4 or 13×10^4 cells cm^{-2} (for wound-healing experiments) and grown for 3–4 d.

Immunostaining: SCs were grown for 3–4 d on FLAT, T1, T4, and T20 PDMS membranes, then fixed for 15 min in 4% paraformaldehyde in phosphate buffered solution (PBS) at room temperature and processed as previously reported.[34] SCs were stained with anti-S100 primary antibody (Sigma; 1:200, rabbit) in GDB buffer (0.2% BSA, 0.8 M NaCl, 0.5% Triton X-100, 30×10^{-3} M phosphate buffer, pH 7.4) containing phalloidin-Alexa647 (Invitrogen A22287; 1:40) to stain actin fibers (F-actin), overnight at 4 °C. Samples were then washed in PBS and incubated with the AlexaFluor488-conjugated secondary antibody (Invitrogen; 1:150, rabbit) in GDB for 2 h at room temperature. After washing, samples were mounted using Vectashield mounting medium with DAPI to stain nuclei (Vector Laboratories). For N-Cad immunostaining, SCs were incubated with anti-N-Cad antibody (BD Transduction Laboratories; 1:250, mouse) together with the anti-S100 antibody in GDB, and then processed with an AlexaFluor647-conjugated

secondary antibody (Invitrogen; 1:150, mouse). Control experiments were also performed on SCs with the anti-CD90 antibody (1:250; AbD Serotec), to check the fibroblast contamination level (Figure S1, Supporting Information).

Confocal Imaging and Cell Morphological Analysis: Confocal images were acquired using a laser scanning confocal microscope TCS SP2 (Leica Microsystems, Germany) with a 40× oil objective by using UV (405 nm), argon (488 nm), and helium (647 nm) lasers. Each reported confocal image was obtained from a *z*-series (stack depth was within 10 μm; steps = 0.5–1 μm). The resulting *z*-stack was processed by ImageJ software (NIH, USA) into a single image using "z-project" and "Max intensity" options. The confocal settings were kept the same for all scans when fluorescence intensity was compared. The confocal images of S-100 (specific SC marker) and DAPI staining were used to evaluate cellular and nuclear morphology by ImageJ. Cell and nucleus contours were drawn by the "Freehand selection" tool and processed by the "Measurement" tool (with the options "Area," "Fit ellipse," and "Feret's diameter"). The orientation of the GR patterns was measured by the "Angle tool" of ImageJ; for FLAT membranes a random direction was chosen. The parameters measured in this analysis were: SC and nucleus area (μm^2); SC and nucleus aspect ratio (the ratio between the length of the major axis and the minor axis for the best-fitted ellipse of the cell or nucleus);[35] SC and nuclear alignment angle (angles were calculated as the absolute value of the difference between the orientation angle of the grating and of the cell/nuclear major axis). SCs/nuclei were considered aligned to the grating if the alignment angle was between 0° and 15° and perpendicular if the latter was between 75° and 90°; the amount of aligned or perpendicular SCs/nuclei was reported as the percentage over the total number. At least 40 cells and 30 nuclei were analyzed per condition. SC cytoskeleton organization was quantified by analyzing the F-actin fluorescence signal with the "Directionality" tool of the software FIJI (http://fiji.sc/Fiji), similar to ref. [34]. This plug-in returned a directionality histogram by exploiting image fast Fourier transform (FFT) algorithms: isotropic images generate a flat histogram, whereas oriented images give a peaked histogram. These histograms were finally fitted by Gaussian curves that returned two parameters, dispersion and directionality (the standard deviation and the center of the Gaussian curve, respectively), the first representing the degree of orientation of the image, the second the direction in which it is oriented (here normalized to the GR pattern orientation direction). We analyzed at least 12 fields/sample; image dimensions were kept fixed to $187 \times 187 \ \mu m^2$.

Cell–Cell Interaction Analysis: The N-Cad signal was acquired by confocal fluorescence and its intensity was quantified as follows: the area covered by SCs was first manually selected for each image as a region of interest (ROI) on the S100-positive image; then the ROI was applied the correspondent N-Cad positive image and N-Cad intensity was measured by the ImageJ "Measure" tool (option "mean gray value"). The values were then reported as percentage over the FLAT substrate. N-Cad signal was also analyzed by the Directionality tool of Fiji as described above for F-actin cytoskeleton organization analysis; at least six images ($150 \times 150 \ \mu m^2$)/sample were analyzed.

Single-Cell Migration Experiments: SCs were cultured on FLAT, T1, T4, and T20 PDMS membranes for 24 h. Bright-field living-cell imaging was performed (at least after 8 h from seeding) using a 20× air Nikon objective (NA 0.45, Plan-Fluor) and Eclipse Ti inverted wide-field microscope (Nikon, Japan) equipped with a perfect focus systems, an incubating chamber (Okolab, Italy), and a CCD ORCA R2 (Hamamatzu, Japan). Images were acquired for 24 h, sampling every 15 min. Movies were analyzed with the ImageJ manual tracking plug-in MTrack. The coordinates of single cells (at least 25 cells/sample) as a function of time were extracted and analyzed by a custom-made Matlab script. The following parameters were measured: migration step (dS; corresponding to the cell motion calculated in 15 min): step vectors were analyzed along two directions, and dS was considered parallel (dS) if the angle between the step and the grating was between 0° and 15°, while it was considered perpendicular (d$S_\perp$) for angle between 75° and 90°; the amount of parallel or perpendicular dS was reported as percentage over the d$S_\parallel$ total number. Cell displacement (R, the distance, in μm, from the origin after 17 h; at least ten cells/sample were averaged). Average cell speed (V, in μm h^{-1}); as previously for dS, the average speed was also quantified as parallel ($V_\parallel$) and perpendicular ($V_\perp$).

Wound-Healing Experiments: Wound-healing measurements were performed on monolayers of SCs, on FLAT and GR membranes. A scratch (average size $W_{mean} = 660 \pm 170$ μm, mean ± SD) perpendicular to the pattern (or along a random direction in the case of FLAT membranes) was performed using a Gilson pipette tip; for each experiment, data were considered valid if the starting wound width was within ±25% of W_{mean}. Images were acquired every hour using a Nikon-Ti wide-field microscope (see above) by using a 4×, 0.1 NA long-distance objective (Plan Achromat, Nikon). 24 h wound-healing time series were recorded by time-lapse microscopy and the wound area was measured after 24 h. The percentage of area closure was finally reported. The number of scattered SCs in the wound at 24 h was also quantified and reported as number of scattered cells/wound area (in mm^2). The contribution of SC proliferation to the wound-closure process is negligible, because the SC proliferation rate is significantly greater than 24 h.

SEM Imaging: Schwann cells were cultured on PDMS membranes, fixed with 2.5% glutaraldehyde in sodium cacodylate buffer (pH 7.2, 0.15 M) for 1 h and successively rinsed three times with sodium cacodylate buffer. Then, the samples were dehydrated with absolute ethanol at different concentrations: 50%, 70%, and 98%, as in ref. [32]. The substrates were then loaded into an LEO 1525 field emission SEM equipped with a charge compensator, and image acquisition was carried out by secondary electron detection with the Everheart–Thornley detector.

Statistical Analysis: All the experiments were repeated at least three times independently for each condition. Data are reported as the average value ± the standard error of the mean (mean ± SEM), unless differently stated. Data were statistically analyzed by using GraphPad Prism commercial software. The mean values obtained in each repeated experiment were assumed to be normally distributed about the true mean. One-way ANOVA (Dunnett's multiple comparison test) analysis was used, unless differently stated, to compare GR substrates to the FLAT control condition. Student's *t*-test (two-tailed, unpaired) was performed

to compare the different GRs. Statistical significance refers to results where $P < 0.05$ was obtained.

3. Results

3.1. Cell Morphological Analysis

PDMS membranes were microfabricated and patterned with anisotropic topographies to direct and improve Schwann cells polarization and migration. Different GR geometries were produced characterized by period of 1 (T1), 4 (T4), and 20 μm (T20) (**Figure 1**, first row); the grating depth was 0.35, 0.85, and 2.5 μm, respectively. PDMS membranes with flat surfaces (FLAT) were used as control substrates.

G iven the typical PDMS hydrophobicity (contact angle ≈100°),[29] the substrates were coated with poly-L-lysine and laminin (0.01% and 50 μg mL^{-1}, respectively) to allow good SC adhesion and spreading. Other surface coatings (e.g., poly-D-lysine, poly-L-lysine alone, or collagen type I) did not sustain SC adhesion and growth (Figure S2, Supporting Information).

In order to study how these patterns affect SC cellular and nuclear morphology, primary rat SCs were cultured on FLAT, T1, T4, and T20 membranes, stained for S100 (SC marker), DAPI (nuclear marker), and phalloidin (actin marker). Cell and nucleus morphological parameters and alignment to the GR lines were then evaluated (**Figure 2**). We initially analyzed the response of individual SCs by measuring the cell shape, cell-body orientation, and alignment to the pattern, as depicted in **Figure 3**a. SC spreading area was the same for all the topographies (1360 ± 220, 1440 ± 30, 1460 ± 20, and 1250 ± 270 μm^2 on FLAT, T1, T4, and T20, respectively). SCs cultured on GRs showed
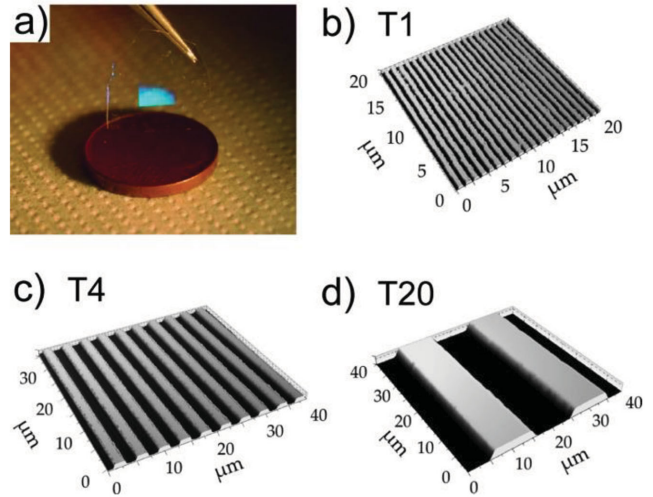

Figure 1. a) PDMS nano/microstructured membranes. b–d) Optical profiles of the different GRs tested in our experiments. Z-scales are 350 nm, 850 nm, and 2.5 μm for T1, T4, and T20, respectively.

increasing body elongation with the increase of the pattern period. In particular, elongation resulted markedly modified for T20 ($P < 0.05$ FLAT vs T20) (Figure 3b). As expected, the SCs aligned to all the GRs (Figure 3c), reducing the alignment angle with the increase of the pattern period ($P < 0.01$ FLAT vs T1; $P < 0.001$ FLAT vs T4 and T20). On FLAT substrates, fully spread SCs displayed a star-like shape and random orientation while the interaction with GRs biased cell orientation, resulting in an average alignment angle of 21.1 ± 4.5° on T1, 13.1 ± 3° on T4, and 6.4 ± 0.8° on T20; here, T20 performed better than T1
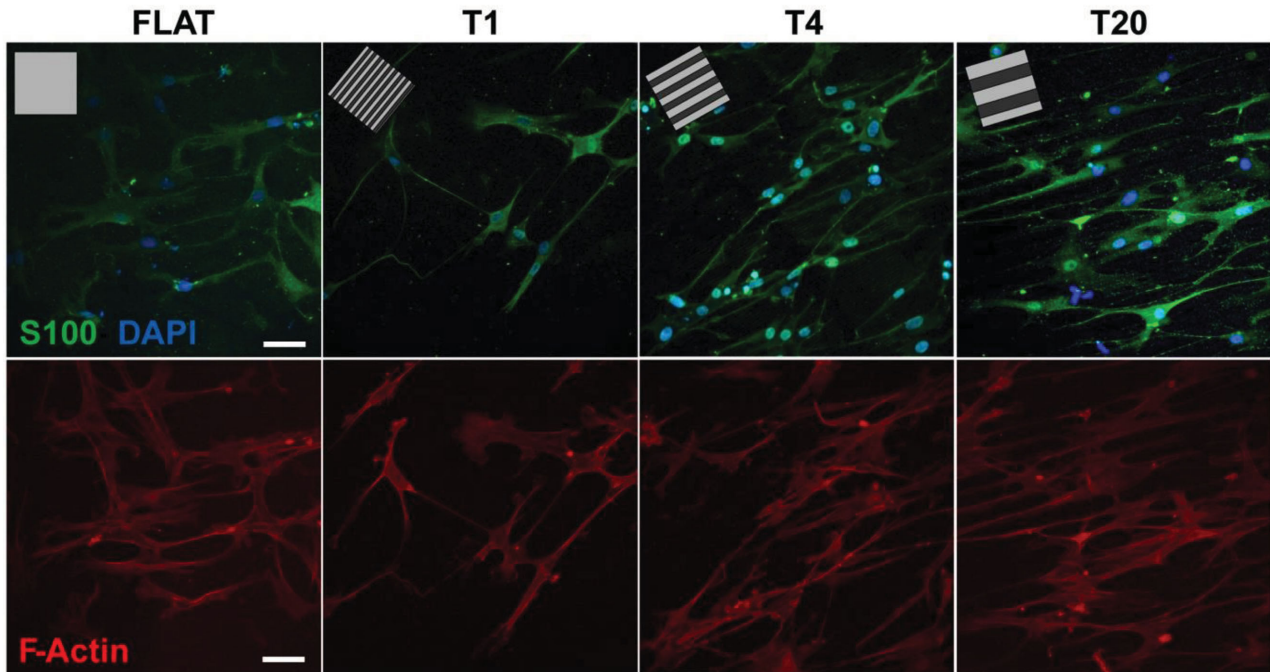

Figure 2. Confocal microscopy images of SCs grown on FLAT, T1, T4, and T20 and stained for S100 (green), nuclei (blue) (first row), and F-actin (red) (second row). Insets: GR pattern direction; scale bar = 50 μm.
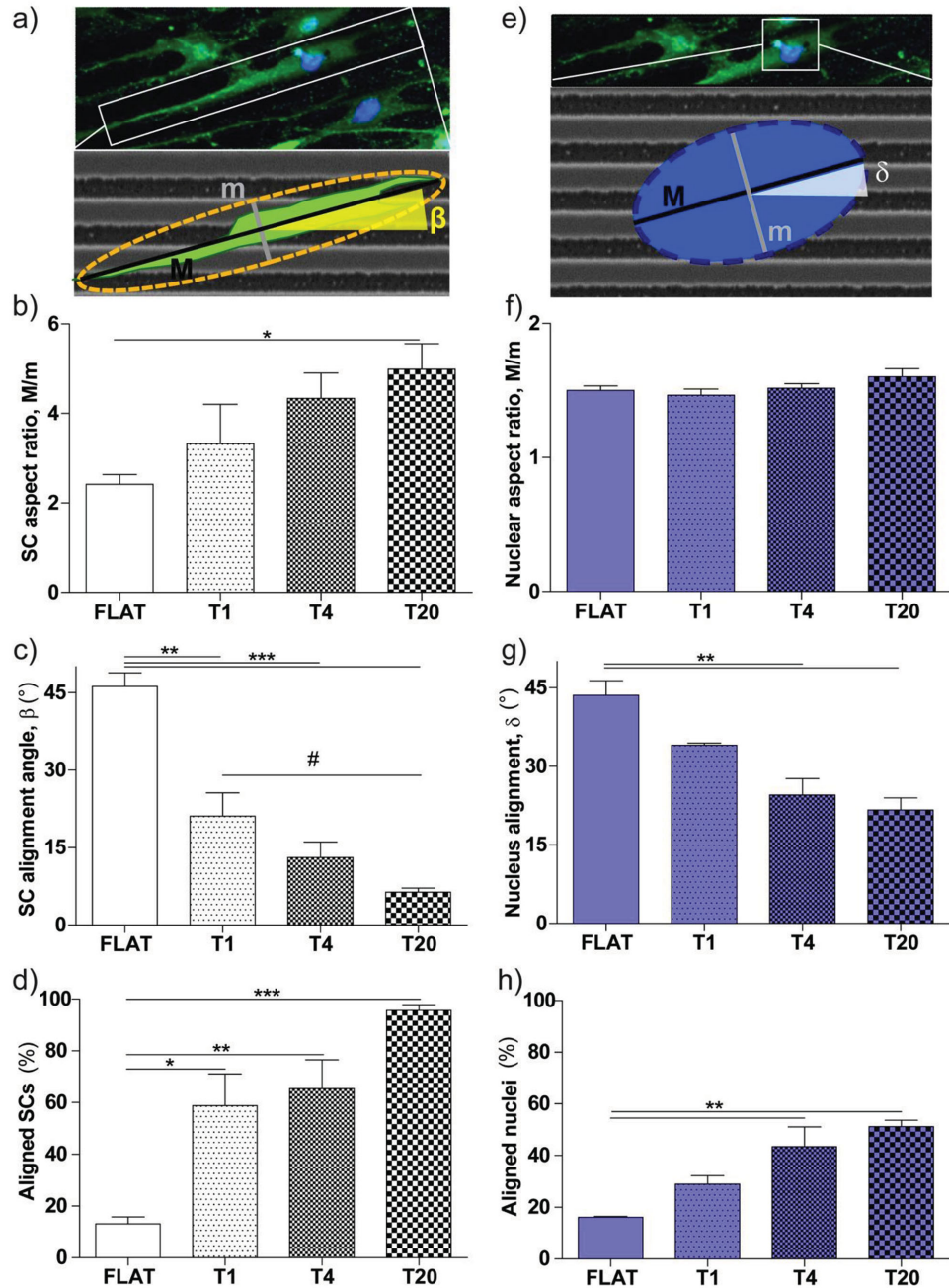
Figure 3. SC cellular and nuclear morphological characterization. The morphometric analysis was performed by manually tracking cell and nucleus shape on a) S100- and e) DAPI-labeled confocal images, respectively. Aspect ratio is the ratio of the length of the major axis (*M*, in black) with the minor axis (*m*, in gray) for the best-fitted ellipse of the cell (orange dotted line) or nucleus (blue dotted line); cell/nuclear alignment angle (*β*/*δ*) is the angle between the cell/nuclear major axis and the direction of the GR; scale bars = 10 µm. b) SC aspect ratio, c) alignment angle, and d) percentage of aligned SCs on different substrates: */**/***$P < 0.05/0.01/0.001$ versus FLAT; #$P < 0.05$ T20 versus T1, Student's *t*-test. f) Nuclear aspect ratio, g) alignment angle, and h) percentage of aligned nuclei on different substrates: */**$P < 0.05/0.01$ versus FLAT.

($P < 0.05$, Student's *t*-test). In order to fully quantify the effect of the microstructures on SC orientation, the percentage of SCs aligned to the topography (i.e., with alignment angle between 0° and 15°) was calculated. As shown in Figure 3d, the percentage of SCs aligned to the pattern significantly increased for all the GRs if compared with FLAT ($P < 0.05$ vs T1; $P < 0.01$ vs T4; $P < 0.001$ vs T20). Consistently, the percentage of SCs oriented

perpendicularly (i.e., with alignment angle between 75° and 90°) dropped for the GRs ($P < 0.01$ FLAT vs T1, T4, and T20) (Figure S3a, Supporting Information).

Since the position of the nucleus and nuclear reorientation can determine cell polarity and migration,[36] we also investigated the morphological parameters of nuclei (Figure 3e) as we did for cell bodies. Nuclear size was not affected by the different

substrates (170 ± 30, 191 ± 6, 185 ± 10, and 170 ± 4 μm² for FLAT, T1, T4, and T20, respectively) as well as the nuclear aspect ratio (Figure 3f). While nuclei were equally elongated for all substrates, their orientation was modified by the GRs (Figure 3g): nuclear alignment improved by increasing GR periodicity ($P < 0.01$ FLAT vs T4 and T20). As found for SC morphology, also the percentage of aligned nuclei increased by increasing the GR period, from 29 ± 3% for T1 to 43 ± 8% for T4 and 51 ± 2% for T20 (whereas on FLAT it was 16 ± 1%) ($P < 0.01$ FLAT vs T4 and T20) (Figure 3h). Concerning perpendicularly oriented SC nuclei, only T4 and T20 could significantly inhibit the perpendicular alignment ($P < 0.05$ FLAT vs T4 and T20) (Figure S3b, Supporting Information).

Altogether, these data demonstrate that SCs can read the underlying topography and shape according to the GR period. These effects become more pronounced as the GR period increases.

3.2. Actin Cytoskeleton Organization

Next we examined how GRs influence SC cytoskeleton organization by actin staining and confocal microscopy. SCs displayed cortical actin and stress fibers (F-actin) (Figure 2). The F-actin high-resolution fluorescence images confirmed the high degree of cell polarization induced by GRs and the absence of a preferential orientation for cell networks assembled on FLAT (Figure 2). F-actin polarization was quantified by an FFT analysis of the fluorescence images, which returns the signal dispersion and directionality as shown in **Figure 4**a. The F-actin dispersion (an indicator for the angular spread of the actin fluorescence signal) decreased on T4 (12.5 ± 1.5°) and T20 (10 ± 1.3°) with respect to that on FLAT (17.9 ± 2.8°), although only the reduction induced by T20 was statistically significant ($P < 0.05$ FLAT vs T20; Figure 4b). F-actin directionality (an indicator for the overall degree of orientation vs GR direction) was considerably affected by all the NGs (Figure 4c). In fact, it was much less for T1 (12.8 ± 2.8°), T4 (8.1 ± 2.4°), and T20 (5.0 ± 1.4°) than for FLAT control surfaces (44.1 ± 4.2°) ($P < 0.001$ FLAT vs T1, T4, and T20).

Overall, these data demonstrate that PDMS GRs can effectively induce SC actin cytoskeleton polarization, tuning F-actin organization along the GR lines. This effect was particularly marked for the T20 geometry.

3.3. Single-Cell Migration Analysis

The ability of SCs to migrate along the GR lines was assessed first by single-cell migration experiments. SCs were cultured on FLAT, T1, T4, and T20 substrates and their motion was followed for 24 h by time-lapse bright-field microscopy (**Figure 5**a). Like other cell types contacting similar gratings, SCs migrated parallel to the direction of the topography, while on FLAT migration was random, with no overall directional preference. The percentage of parallel steps increased progressively with the increase of GR periodicity (Figure 5b) from 19 ± 1% for FLAT (for random motion with an arbitrary reference direction, the percent of aligned steps would theoretically be ≈20%) to 28 ± 5.0% for T1, 37 ± 3% for T4
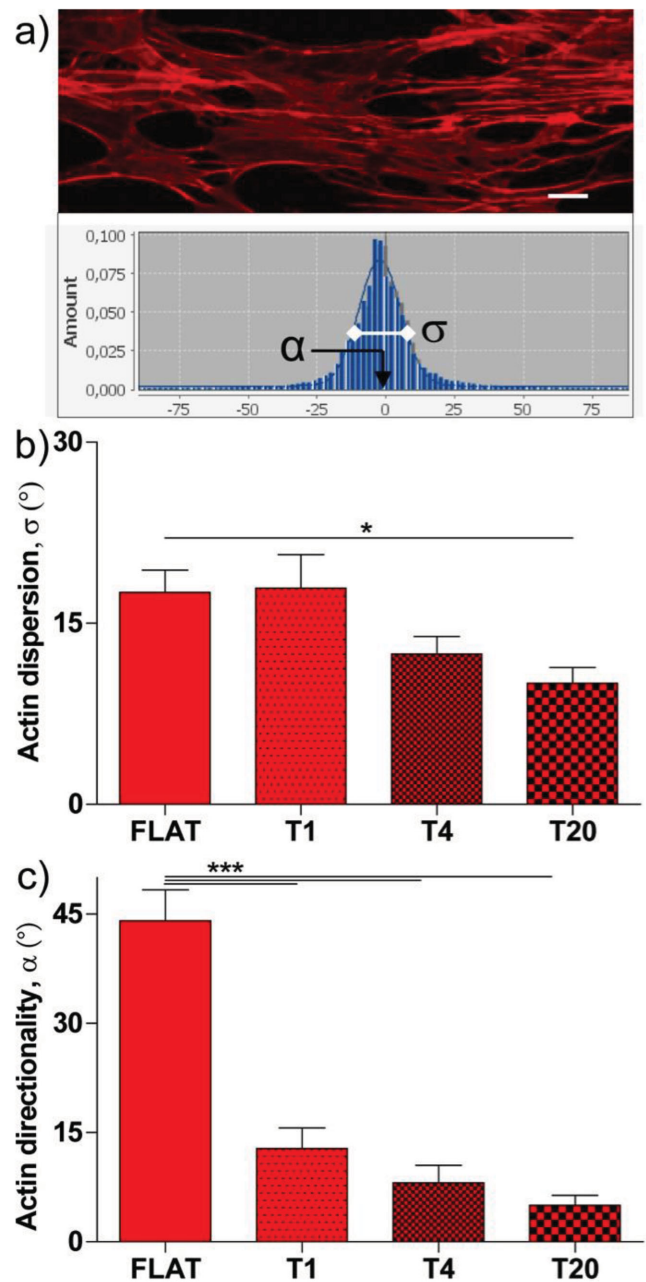

Figure 4. F-actin cytoskeleton polarization analysis. a) Representative F-actin confocal image (left) and relative image fast Fourier transform (FFT) (right); scale bar = 10 μm. b) F-actin dispersion (σ) calculated for the different substrates: *$P < 0.05$ T20 versus FLAT. b) F-actin directionality (α) calculated for the different substrates: ***$P < 0.001$ T1, T4, and T20 versus FLAT.

($P < 0.01$ vs FLAT) and 46 ± 5% for T20 ($P < 0.001$ vs FLAT). Conversely, there was a decrease in the quantity of perpendicular steps (Figure 5c): SC migration perpendicular to the pattern was highly suppressed for all GRs with respect to FLAT surfaces and in particular for T4 and T20 ($P < 0.01$ vs T1; $P < 0.001$ vs T4 and T20). Finally, we quantified SC displacement at $t = 17$ h (R) (Figure 5d). Generally, GR topographies had a positive effect on R, which originated by the anisotropic directional migration along the patterns.
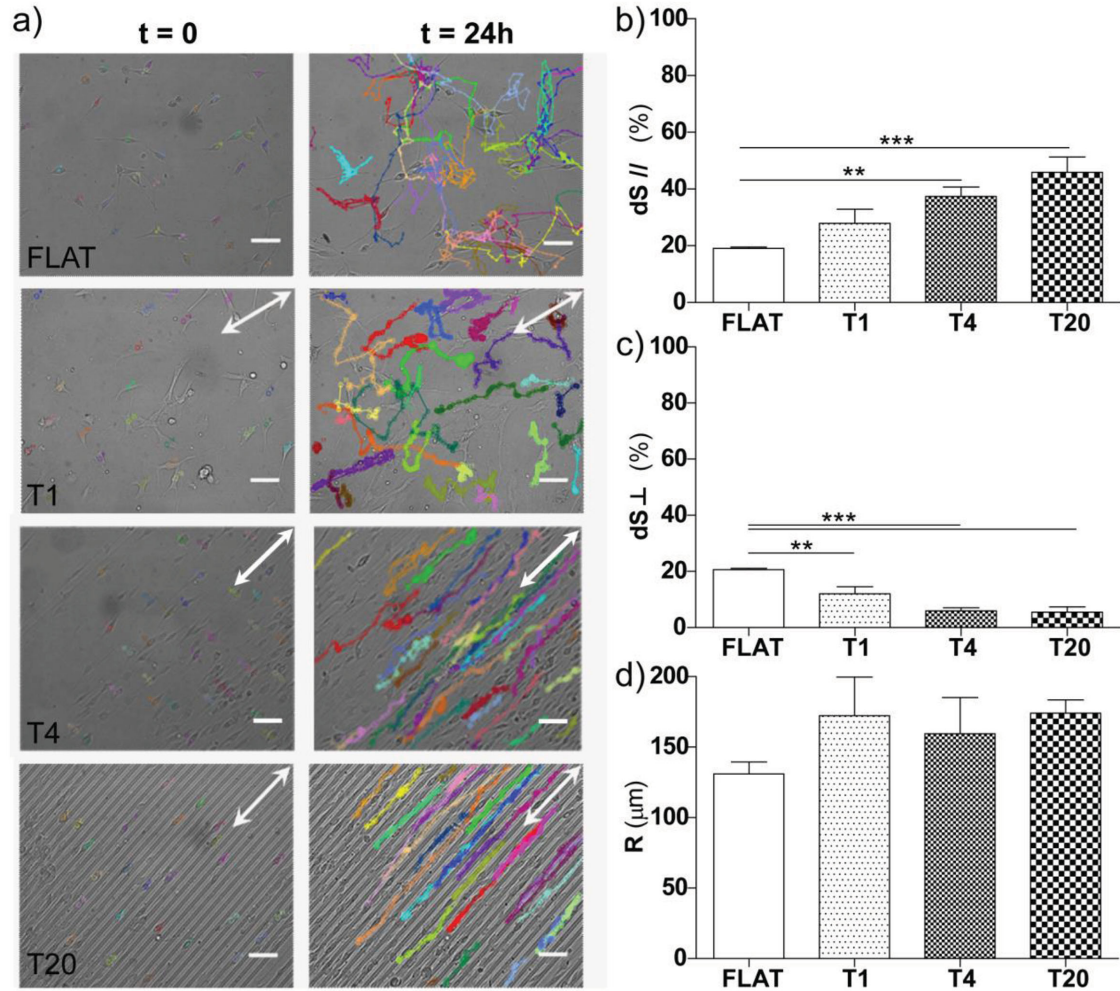
Figure 5. Single-cell migration analysis. a) Representative bright-field images of SC migration patterns (colored tracks) on FLAT, T1, T4, and T20 PDMS substrates. White arrows represent the pattern direction; scale bars = 50 µm. Percentage of steps b) parallel $dS_\parallel$ and c) perpendicular $dS_\perp$ to the pattern orientation for each substrate: **/***$P < 0.01/0.001$ versus FLAT. d) SC final displacement R (at $t = 17$ h) from the $t = 0$ position on different substrates.

The mean overall migration speed was nearly the same on FLAT ($V = 28 \pm 3$ µm h^{-1}) and GR membranes ($V = 27 \pm 3$, 29 ± 2, and 29 ± 1 µm h^{-1}, on T1, T4, and T20, respectively) (Figure S4a, Supporting Information). In order to further describe the directional nature of single-cell migration, we selectively analyzed the velocity in its perpendicular and parallel components ($V_\perp$ and $V_\parallel$, respectively). T4 and T20 enhanced $V_\parallel$ and reduced $V_\perp$: $V_\parallel$ was greater than $V_\perp$ both for T4 and T20 ($P < 0.001$ $V_\parallel$ vs $V_\perp$, Student's t-test) (Figure S4b, Supporting Information).

Altogether, these data demonstrate that all the tested topographies, but in particular T4 and T20, are effective in polarizing single SC migration, favoring cell motion along the GR lines.

3.4. SC Wound Healing on GRs

The collective migration of SCs from the proximal to the distal stump is a crucial event during nerve regeneration. Therefore, the ability of SCs to collectively migrate toward an open space along GRs was assessed in vitro, by 24 h wound-healing experiments. Wounds were mechanically inflicted to SC monolayers perpendicular to the GRs and along a random direction on FLAT surfaces. As shown in **Figure 6**a, wound healing was favored by GRs with respect to the FLAT condition. Interestingly, wound closure proceeded more efficiently on T4 ($P < 0.01$) than on T20 (Figure 6b).

In order to further investigate the reason why the T20 was not the best performing GR in closing the monolayer gap as it was for single-cell polarization and migration, we quantified the scattered SCs present in the wound at $t = 24$ h. Figure 6c demonstrates that the number of scattered SCs in the wound area is much increased in T20 (78 ± 15 cells mm^{-2}) compared to FLAT (21 ± 9 cells mm^{-2}; $P < 0.05$), but this is not the case with T4 (46 ± 9 cells mm^{-2}).

These data indicate T4 as the most effective pattern for collective migration and wound-healing performance. Interestingly, although T20 performed best for single-cell polarization and migration, in the wound-healing assay it did not improve SC collective migration. Conversely, it led to enhanced single-cell scattering into the wound.
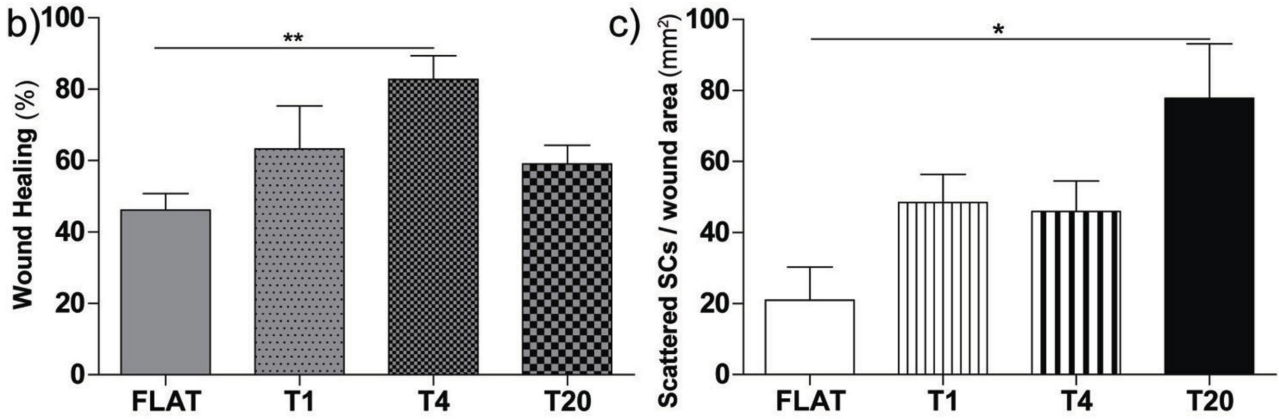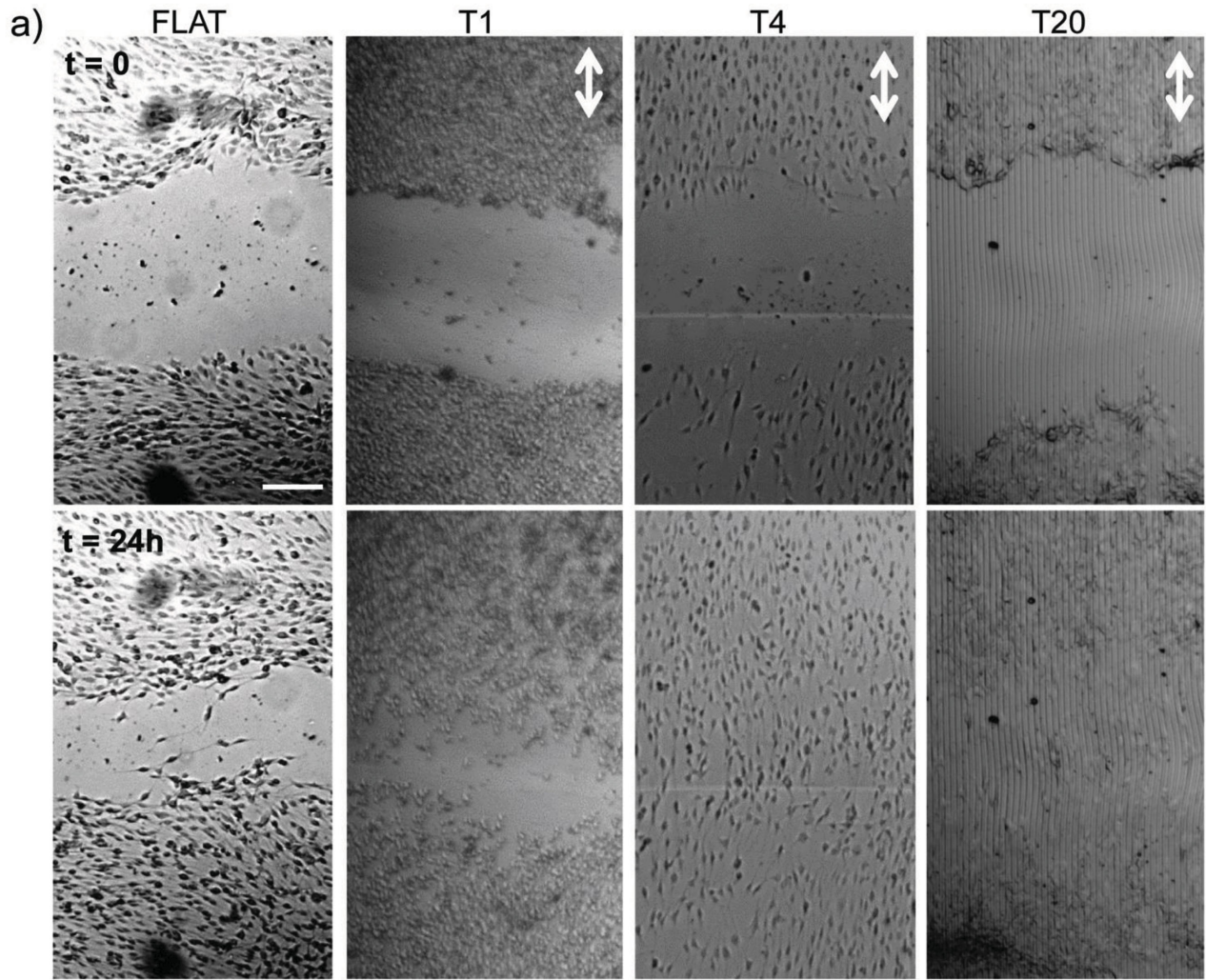
Figure 6. SC wound-healing analysis. a) Representative bright-field images of SC collective migration on FLAT, T1, T4, and T20 substrates, immediately after the scratch ($t = 0$) and at $t = 24$ h; white arrows = GR direction; scale bar = 200 μm. b) Wound closure (%) at $t = 24$ h: **$P < 0.01$ T4 versus FLAT. c) Number of single SCs scattered into the wound area at $t = 24$ h: *$P < 0.05$ T4 versus FLAT.

3.5. SC Contact Interactions in Cell Monolayers

For a deeper understanding of the mechanisms leading to the observed collective cell migration characteristics, we evaluated to what extent the presence of GRs modified SC contact interactions in cell monolayers.

First, SCs were cultured until confluence and then imaged by SEM (**Figure 7**). While on T1 and T4 cells extensively contacted one another (Figure 7a,b), on T20 they were more confined on ridge or groove tracks (Figure 7c). This spatial arrangement may stem from weaker cell–cell contacts on T20 with respect to those on the other substrates. SEM images also highlight how
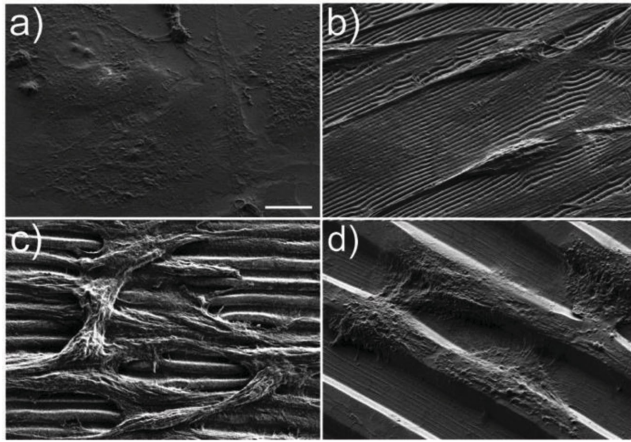
Figure 7. Representative scanning electron microscopy images of SCs grown on a) FLAT, b) T1, c) T4, and d) T20; scale bar = 10 µm.

the traction forces applied to the substrates by the adhered SCs could bend the PDMS grating lines.

SCs monolayers were immunostained for N-Cad in order to evaluate N-Cad expression as marker of cell–cell contact interaction level. Cadherins have a primary role in modulating cell–cell junctions, proliferation, and migration: in particular, N-Cad is involved in glia–glia and axon–glia interactions and participates in many key events, which range from cell polarization and migration to the control of axonal guidance and growth.[37,38] Confocal imaging shows that N-Cad was mainly localized at membrane protrusions and at cell–cell junctions (**Figure 8**). The localization of N-Cad was modified on GRs with respect to FLAT, as it developed oriented and aligned to micropatterns (Figure 8b/d), while it appeared randomly organized on FLAT (Figure 8a). In fact, the directionality and dispersion of the fluorescence signal correlated with those measured for F-actin cytoskeleton (Figure 4b,c): the dispersion was significantly reduced on T4 and T20 ($P < 0.05$ and $P < 0.01$ vs FLAT, respectively), and the directionality angle dropped for all the GRs ($P < 0.001$ FLAT vs T1, T4, and T20) (Figure S5a,b, Supporting Information). Finally, the N-Cad signal intensity was quantified (see the Experimental Section for details). The expression of N-Cad was undistinguishable between T4 and FLAT, while it resulted slightly suppressed with T1 and T20. In particular, a direct comparison between T4 and T20 showed significant N-Cad downregulation on T20 ($P < 0.05$ T4 vs T20, Student's t-test) (Figure 8e).

Altogether these data show N-Cad polarization in SC monolayers contacting all the GRs that correlates with actin polarization. Importantly, the quantitative analysis of N-Cad fluorescence intensity indicates that N-Cad expression on T20 is down-regulated with respect to that on T4.

4. Discussion

In the present work, we tested the ability of GR-patterned PDMS polymeric membranes to control and direct Schwann cell shaping and migration, with the aim to evaluate these geometries for nerve-regeneration applications. We examined
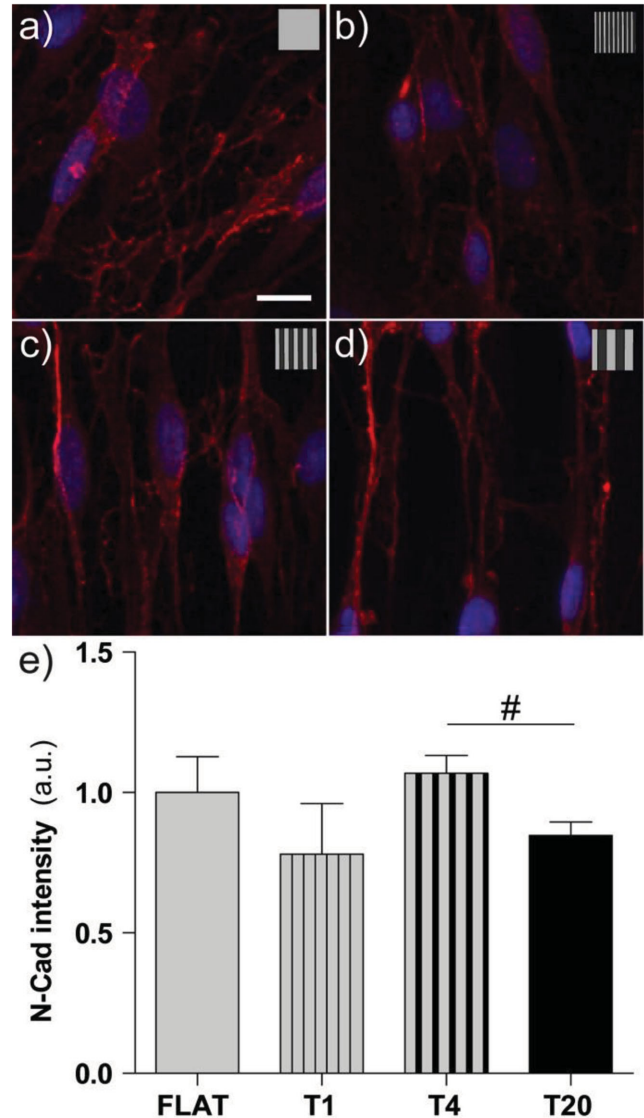

Figure 8. Confocal images of SCs grown on a) FLAT, b) T1, c) T4, and d) T20 and immuno-fluorescently labeled for N-Cad (red); nuclei are shown in blue (DAPI staining). Insets = GR pattern direction; scale bar = 10 µm. e) N-Cad quantitative analysis. N-Cad fluorescence intensity is reported normalized to the value measured on FLAT: #$P < 0.05$ T4 versus T20, Student's t-test.

the response of primary rat SCs to GRs with period ranging from 1 to 20 µm and depth from 0.35 to 2.5 µm, in terms of morphology, actin cytoskeleton organization, single and collective migration, and cell–cell interaction.

Our data show that cell and nuclear shapes and cytoskeleton organization did respond to the GR according to the pattern periodicity. Actin cytoskeleton was polarized along the GR lines, and the nucleus was oriented as well (Figures 3 and 4). These effects, measured for single cells, correlated and were more pronounced for the larger periodicities studied. Nuclear movements are mediated by the cytoskeleton, which transmits pushing or pulling forces onto the nuclear envelope.[39] In fact, it has been demonstrated by nanopillar arrays the central role

of actin filaments in inducing nuclear deformation in several cells.[40] Although the functional significance of nuclear dynamic regulation is not always evident, it is known that in motile cells that polarize for migration, the nucleus rotates to align its major axis with the direction of migration.[36] Consistently, our data show that single SC migration was oriented along the GR lines, with increasing efficiency with the increase of the GR period. Beyond migration, actin cytoskeleton and, in general, cell contractility are actively involved in many other cellular processes that are central for nerve regeneration. For example, myosin II-mediated contractility directly acts on actin stress fiber formation[41] and it was reported to regulate neuron polarity selection during differentiation.[21] Contractility also regulates actin cytoskeleton organization during SC differentiation and myelination.[42] Moreover, in myosin II–null SCs the failure to myelinate the axons during regeneration was linked to the inability of SCs to orient their cytoskeleton and directionally move following the cues coming from axons and the extracellular matrix.[42,43] This evidence points at positive effects on myelination during regeneration as a result of GR-driven enhanced SC polarization and actin organization.

Unexpectedly, collective migration upon wound healing was instead significantly enhanced only on T4, while we found similar performance on T20, T1, and FLAT. Importantly, single SC scattering into the wound healing area was instead favored by T20. Thus, in order to assess the cohesiveness of the cell monolayers developed on the different GRs, we quantified N-Cad expression by fluorescence microscopy and found downregulation in cells on T20 with respect to those on T4. Altogether, our data suggest that T20, while performing best for single-cell polarization and migration, could not support strong cell–cell junctions; single-cell scattering from the wound edges was then favored and this negatively affected the performance in collective cell migration and wound closure. This scenario is confirmed by SEM imaging (Figure 7), which revealed that SCs on T20 tend to be confined on ridges or inside grooves rather than form a homogeneous cell carpet.

An important aim of tissue engineering is to reach a full control over the most important cellular functions, including proliferation, differentiation, cell–cell interactions, and motility. This can be obtained in part by properly tailoring the materials upon which cells are grown. In our previous studies, we showed that GRs can be exploited to promote neuronal polarization and migration, and neurite alignment. These substrates can impose a geometrical constrain to focal adhesion maturation acting on the ROCK-mediated contractility pathway.[16,21,44–46] Beyond neurons, addressing specific aspects of SC motility on GRs completes the picture and add relevant information for novel biomaterial-based strategies to enhance nerve regeneration.[47] After injury, SCs align longitudinally in columns to promote the regrowth of injured axons, leading to axonal alignment in their direction.[48] For this reason, the improvement of SC migration is a strategy to accelerate the creation of this highly ordered SC matrix, and the following regrowth of neurons. It was demonstrated that not only neurite growth follows the underlying SC structure, but the presence of oriented SCs facilitates neurite alignment and orientation.[49–51] In our experiments, SCs were observed to keep moving in a specific direction (parallel to the GRs) for longer distance than they would have with no

topographical cues (Figure 6). This did affect migration velocity components selectively (parallel was enhanced and perpendicular decreased) thus leading to straighter paths (Figure S4, Supporting Information), yet no effect on the overall migration speed was measured. In agreement with our data, Mitchel[52] found that topography had stronger effects on SC directional behavior than on their migration velocity on their large-period (30 µm linewidth) microgrooved substrates.

Similarly, few other microgrooved surfaces were investigated for nerve-repair applications, mostly in vitro and, very recently, in vivo.[53,54] The main difference with the geometries presented in our study is the lateral period. Indeed, existing approaches are based on larger grating lines, of the order of 10 µm and more.[50,55–58] These authors interfaced SCs or immortalized SC-like cellular lines with this kind of GRs, which acted on cells by boundary guidance (i.e., grating period ≥ cell body diameter).[52,53] However, to the best of our knowledge, a complete study on cell collective and/or functional responses (e.g., collective migration, cell layer quality) was never reported before this study. As shown by our results on T20, the boundary guidance may not be optimal to improve nerve regeneration, while GRs that work in the contact guidance regime (i.e., grating period = cell body diameter),[10,16,59] such as our T4, are expected to be more efficient to direct collective cell migration and favor cell–cell interactions. Figure 8 indeed shows that T20 and T4 induced different N-Cad expression, while both similarly modifying N-Cad spatial organization (Figure S5, Supporting Information). It is known that N-Cad removal from the SC surface can result in failure of SCs to form networks and reduce their ability to align with axons;[30] moreover, its expression increases after nerve injury, thus allowing active regeneration.[31] Therefore, N-Cad reduction in cells on T20 may account for the degraded performance in terms of collective migration that we measured for SCs on T20 with respect to those on T4, and for the high number of scattered cells into the wound recorded on T20 (Figure 6c). Instead, T4 showed high and polarized N-Cad expression, a configuration consistent with improved collective migration.[60] Interestingly, spatially oriented N-Cad networks are present along the SC–axon interfaces in vivo,[30,61] suggesting that our substrates may also promote more physiological nerve regrowth than unpatterned conduits.

5. Conclusions

In conclusion, we studied the effect of microtextured substrates on SC morphology and function as driven by pure contact interaction in view of possible use for nerve-repair applications. PDMS GRs were developed with different lateral periods and depths, leading to two distinct cell–substrate interaction regimes: contact guidance (grating period < cell body diameter, obtained for T1 and T4) and boundary guidance (grating period ≥ cell body diameter, obtained for T20).

The analysis of single SCs revealed important variations following GRs contact interaction, regardless the interaction regime. Specifically, T20 performed best among all tested GRs, showing the best SC aspect ratio and alignment, nuclear alignment, actin organization, and single-cell directional migration. Conversely, wound-healing experiments demonstrated

that contact guidance can be more effective in driving collective SC migration than boundary guidance. Indeed, T4 could significantly improve wound-closure speed, while we did not find any significant difference between T20 and the flat control substrate. We linked this behavior to the properties of the SC monolayers generated by the different GRs. SCs on T20 were indeed characterized by N-Cad downregulation and enhanced single-cell scattering into the wound with respect to SCs developing on T4, suggesting a less compact monolayer characterized by looser cell–cell junctions. Overall T4 (with 4 μm period and 0.85 μm depth) emerged as the most effective of the topographies studied in tuning SC directional orientation and migration. Our results provide information of the impact of specific topographical elements that can be exploited for tissue engineering applications and for the production of new devices enhancing peripheral nerve regeneration.

Supporting Information

Supporting Information is available from the Wiley Online Library or from the author.

[1] P. L. Williams, in *Gray's Anatomy*, 38th ed., *Nervous System* Vol., Churchill Livingstone, London, UK **1999**.

[2] M. Siemionow, G. Brzezicki, *Int. Rev. Neurobiol.* **2009**, *87*, 141.

[3] W. Daly, L. Yao, D. Zeugolis, A. Windebank, A. Pandit, *J. R. Soc. Interface* **2012**, *9*, 202.

[4] M. P. Tohill, G. Terenghi, *Biotechnol. Appl. Biochem.* **2004**, *40*, 17.

[5] S. Kehoe, X. F. Zhang, D. Boyd, *Injury* **2012**, *43*, 553.

[6] B. Battiston, S. Raimondo, P. Tos, V. Gaidano, C. Audisio, A. Scevola, I. Perroteau, S. Geuna, *Int. Rev. Neurobiol.* **2009**, *87*, 227.

[7] S. Raimondo, M. Fornaro, P. Tos, B. Battiston, M. G. Giacobini-Robecchi, S. Geuna, *Ann. Anat.* **2011**, *193*, 334.

[8] W. T. Daly, L. Yao, M. T. Abu-rub, C. O'Connell, D. I. Zeugolis, A. J. Windebank, A. S. Pandit, *Biomaterials* **2012**, *33*, 6660.

[9] D. Hoffman-Kim, J. A. Mitchel, R. V. Bellamkonda, *Annu. Rev. Biomed. Eng.* **2010**, *12*, 203.

[10] B. Geiger, J. P. Spatz, A. D. Bershadsky, *Nat. Rev. Mol. Cell Biol.* **2009**, *10*, 21.

[11] A Webb, P. Clark, J. Skepper, A. Compston, A. Wood, *J. Cell Sci.* **1995**, *108*, 2747.

[12] N. Gomez, S. Chen, C. E. Schmidt, *J. R. Soc. Interface* **2007**, *4*, 223.

[13] E. Schnell, K. Klinkhammer, S. Balzer, G. Brook, D. Klee, P. Dalton, J. Mey, *Biomaterials* **2007**, *28*, 3012.

[14] M. J. P. Biggs, R. G. Richards, M. J. Dalby, *Nanomedicine* **2010**, *6*, 619.

[15] I. Tonazzini, E. Bystrenova, B. Chelli, P. Greco, P. Stoliar, A. Calò, A. Lazar, F. Borgatti, P. D'Angelo, C. Martini, F. Biscarini, *Biophys. J.* **2010**, *98*, 2804.

[16] A. Ferrari, M. Cecchini, A. Dhawan, S. Micera, I. Tonazzini, R. Stabile, D. Pisignano, F. Beltram, *Nano Lett.* **2011**, *11*, 505.

[17] S. Persheyev, Y. Fan, A. Irving, M. J. Rose, *J. Biomed. Mater. Res. A* **2011**, *99*, 135.

[18] L. Cai, L. Zhang, J. Dong, S. Wang, *Langmuir* **2012**, *28*, 12557.

[19] S. Eshghi, D. V Schaffer, C. Engineering, *StemBook* **2008**, 1.

[20] F. Guilak, D. M. Cohen, B. T. Estes, J. M. Gimble, W. Liedtke, C. S. Chen, *Cell Stem Cell* **2009**, *5*, 17.

[21] A. Ferrari, M. Cecchini, M. Serresi, P. Faraci, D. Pisignano, F. Beltram, *Biomaterials* **2010**, *31*, 4682.

[22] A. Ferrari, P. Faraci, M. Cecchini, F. Beltram, *Biomaterials* **2010**, *31*, 2565.

[23] I. Tonazzini, A. Cecchini, Y. Elgersma, M. Cecchini, *Adv. Healthcare Mater.* **2013**, *3*, 581.

[24] C. Di Rienzo, E. Jacchetti, F. Cardarelli, R. Bizzarri, F. Beltram, M. Cecchini, *Sci. Rep.* **2013**, *3*, 1141.

[25] D. Franco, F. Milde, M. Klingauf, F. Orsenigo, E. Dejana, D. Poulikakos, M. Cecchini, P. Koumoutsakos, A. Ferrari, V. Kurtcuoglu, *Biomaterials* **2013**, *34*, 1488.

[26] S. Geuna, S. Raimondo, G. Ronchi, F. Di Scipio, P. Tos, K. Czaja, M. Fornaro, *Int. Rev. Neurobiol.* **2009**, *87*, 27.

[27] S. Hall, *J. Hand Surg. Br.* **2001**, *26*, 129.

[28] J. C. McDonald, D. C. Duffy, J. R. Anderson, D. T. Chiu, H. Wu, O. J. Schueller, G. M. Whitesides, *Electrophoresis* **2000**, *21*, 27.

[29] E. Berthier, E. W. K. Young, D. Beebe, *Lab Chip* **2012**, *12*, 1224.

[30] I. B. Wanner, P. M. Wood, *J. Neurosci.* **2002**, *22*, 4066.

[31] M. R. Thornton, C. Mantovani, M. A. Birchall, G. Terenghi, *J. Anat.* **2005**, *206*, 69.

[32] M. Cecchini, G. Bumma, M. Serresi, F. Beltram, *Nanotechnology* **2007**, *18*, 505103.

[33] A. C. De Luca, G. Terenghi, S. Downes, *J. Tissue Eng. Regener. Med.* **2012**, *8*, 153.

[34] I. Tonazzini, M. Pellegrini, M. Pellegrino, M. Cecchini, *Interface Focus* **2014**, *4*, 20130047.

[35] H. Yu, K. P. Lim, S. Xiong, L. P. Tan, W. Shim, *Adv. Healthcare Mater.* **2013**, *2*, 1188.

[36] M. Maninová, M. P. Iwanicki, T. Vomastek, *Cell Adhes. Migr.* **2014**, *8*, 42.

[37] M. Corell, G. Wicher, C. Limbach, M. W. Kilimann, D. R. Colman, Å. F. Svenningsen, *J. Neurosci. Res.* **2010**, *88*, 2338.

[38] S. Parrinello, I. Napoli, S. Ribeiro, P. W. Digby, M. Fedorova, D. B. Parkinson, R. D. S. Doddrell, M. Nakayama, R. H. Adams, A. C. Lloyd, *Cell* **2010**, *143*, 145.

[39] I. Dupin, S. Etienne-Manneville, *Int. J. Biochem. Cell Biol.* **2011**, *43*, 1698.

[40] L. Hanson, W. Zhao, H. Y. Lou, Z. C. Lin, S. W. Lee, P. Chowdary, Y. Cui, B. Cui, *Nat. Nanotechnol.* **2015**, *10*, 554.

[41] J. T. Parsons, A. R. Horwitz, M. A. Schwartz, *Nat. Rev. Mol. Cell Biol.* **2010**, *11*, 633.

[42] C. Fernandez-Valle, D. Gorman, A. M. Gomez, M. B. Bunge, *J. Neurosci.* **1997**, *17*, 241.

[43] H. Wang, A. Tewari, S. Einheber, J. L. Salzer, C. V. Melendez-Vasquez, *J. Cell Biol.* **2008**, *182*, 1171.

[44] I. Tonazzini, S. Meucci, P. Faraci, F. Beltram, M. Cecchini, *Biomaterials* **2013**, *34*, 6027.

[45] S. Meucci, I. Tonazzini, F. Beltram, M. Cecchini, *Soft Matter* **2012**, *8*, 1109.

[46] P. Wieringa, I. Tonazzini, S. Micera, M. Cecchini, *Nanotechnology* **2012**, *23*, 275102.

[47] V. Lionetti, M. Cecchini, C. Ventura, *Stem Cells Dev.* **2011**, *20*, 561.

[48] J. W. Fawcett, R. J. Keynes, *Annu. Rev. Neurosci.* **1990**, *13*, 43.

[49] J. M. Bruder, A. P. Lee, D. Hoffman-Kim, *J. Biomater. Sci. Polym. Ed.* **2007**, *18*, 967.

[50] C. Miller, H. Shanks, A. Witt, G. Rutkowski, S. Mallapragada, *Biomaterials* **2001**, *22*, 1263.

[51] D. M. Thompson, H. M. Buettner, *Ann. Biomed. Eng.* **2006**, *34*, 161.

[52] J. A. Mitchel, D. Hoffman-Kim, *PLoS One* **2011**, *6*, e24316.

[53] A. Mobasseri, A. Faroni, B. M. Minogue, S. Downes, G. Terenghi, A. J. Reid, *Tissue Eng., Part A* **2015**, *21*, 1152.

[54] A. Srinivasan, M. Tahilramani, J. T. Bentley, R. K. Gore, D. C. Millard, V. J. Mukhatyar, A. Joseph, A. S. Haque, G. B. Stanley, A. W. English, R. V. Bellamkonda, *Biomaterials* **2015**, *41*, 151.

[55] S. Hsu, C.-Y. Chen, P. S. Lu, C.-S. Lai, C.-J. Chen, *Biotechnol. Bioeng.* **2005**, *92*, 579.

[56] M. Sun, M. McGowan, P. J. Kingham, G. Terenghi, S. Downes, *J. Mater. Sci. Mater. Med.* **2010**, *21*, 2765.

[57] J. C. Clarke, B. W. Tuft, J. D. Clinger, R. Levine, L. S. Figueroa, C. A. Guymon, M. R. Hansen, *Hear. Res.* **2011**, *278*, 96.

[58] S. A. Mobasseri, G. Terenghi, S. Downes, *J. Mater. Sci. Mater. Med.* **2013**, *24*, 1639.

[59] C. G. Bettinger, R. Langer, J. T. Borestein, *Angew. Chem. Int. Ed.* **2010**, *48*, 5406.

[60] W. Shih, S. Yamada, *J. Cell Sci.* **2012**, *125*, 3661.

[61] K. A. Lewallen, Y. A. Shen, A. R. De la Torre, B. K. Ng, D. Meijer, J. R. Chan, *J. Neurosci.* **2011**, *31*, 3032.